The Astrophysical Journal, 998:58 (11pp), 2026 February 10 https://doi.org/10.3847/1538-4357/ae2758

A Mysterious Feature in the NICER Spectrum of 4U 1820-30: A Gravitationally Redshifted Absorption Line?

R. Iaria[1], T. Di Salvo[1], A. Anitra[1], F. Barra[1,2,3], A. Sanna[4,5], C. Maraventano[1,6], C. Miceli[1,2,7], W. Leone[1,8,9], and L. Burderi[2,4,5]
[1] Università degli Studi di Palermo, Dipartimento di Fisica e Chimica—Emilio Segrè, via Archirafi 36, Palermo, 90123, Italy; rosario.iaria@unipa.it
[2] Istituto di Astrofisica Spaziale e Fisica Cosmica, Istituto Nazionale di Astrofisica, via Ugo La Malfa 153, Palermo, I-90146, Italy
[3] Center for Astrophysics|Harvard & Smithsonian, 60 Garden Street, Cambridge, MA 02138, USA
[4] Dipartimento di Fisica, Università degli Studi di Cagliari, SPMonserrato-Sestu, KM 0.7, Monserrato (CA), 09042, Italy
[5] Osservatorio Astronomico di Cagliari, Istituto Nazionale di Astrofisica, via della Scienza 5, Selargius (CA), I-09047, Italy
[6] INAF—Osservatorio Astronomico di Brera, Via E. Bianchi 46, I-23807 Merate (LC), Italy
[7] IRAP, Universitè de Toulouse, CNRS, UPS, CNES, 9, avenue du Colonel Roche, Toulouse, 44346, F-31028, France
[8] Dipartimento di Fisica, University of Trento, Via Sommarive, 14, 38123, Povo (TN), Italy
[9] OATS, Via Giambattista Tiepolo, 11, 34131, Trieste (TS), Italy
Received 2025 July 29; revised 2025 November 12; accepted 2025 November 24; published 2026 February 3

Abstract

A mysterious absorption feature at approximately 3.8 keV has been identified in the Neutron star Interior Composition Explorer (NICER) spectrum of the low-mass X-ray binary system 4U 1820-30. We interpret this feature as a gravitationally redshifted iron absorption line. This interpretation is supported by the temporal proximity of the NICER observation to the detection of a carbon superburst—a long and intense thermonuclear flash on the neutron star's surface—by the X-ray monitor MAXI, suggesting that the presence of the line is associated with this rare and extreme event. From the inferred redshift of the absorption line, the compactness of the neutron star can be derived. Fitting this feature with a photoionization absorption model, we measure a redshift of $1 + z \simeq 1.72$, which implies a neutron star compactness of $R/M = 4.46 \pm 0.13\ \mathrm{km}/M_{\odot}$ or 3.02 ± 0.09 in dimensionless units. This unique feature highlights the importance of further observations and detailed modelling, offering promising insights into the equation of state of matter under extreme density conditions.

Unified Astronomy Thesaurus concepts: Low-mass x-ray binary stars (939); Neutron stars (1108); X-ray bursts (1814); Spectroscopy (1558); General relativity (641)

1. Introduction

Neutron stars, remnants of core-collapse supernovae, serve as cosmic laboratories that provide a unique window into the physics of extremely dense matter. These stellar objects, with masses typically around 1.4 times that of the Sun but compressed into a sphere just about 10 km in radius, exhibit conditions unattainable in terrestrial laboratories. The study of neutron stars enriches our understanding of stellar evolution and death and probes matter's fundamental properties under extreme pressures and densities.

Central to the enigma of neutron stars is the equation of state (EoS) of ultra-dense matter, a pivotal yet elusive piece of the astrophysical puzzle. The EoS describes how matter behaves under the extreme conditions found within neutron stars, encompassing pressures and densities beyond nuclear saturation density. This quest to decipher the EoS challenges theoretical physicists and observational astrophysicists, requiring innovative theoretical models and cutting-edge observational techniques (F. Özel & P. Freire 2016).

Recent years have witnessed significant advances in this domain, spurred by the advent of gravitational wave astronomy and high-precision X-ray observations. The detection of gravitational waves from neutron star mergers, such as GW170817, has provided new insights into the stiffness of the neutron star matter EoS and its behavior at supra-nuclear densities (B. P. Abbott et al. 2017). Concurrently, observations from the Neutron star Interior Composition Explorer (NICER) have offered new information on neutron star masses and radii, further constraining the possible EoS models (see, e.g., T. E. Riley et al. 2019).

Among the most promising yet challenging methods to disclose information on the EoS of neutron stars is the detection of spectral lines from (close by) their surfaces. The gravitational redshift observed in these lines serves as a direct probe into the compactness of neutron stars. The initial detection of gravitationally redshifted iron and oxygen absorption lines in the X-ray spectrum of the neutron star in EXO 0748-676 during type I bursts marked a milestone in the study of ultra-dense matter (J. Cottam et al. 2002). However, subsequent observations have yielded inconclusive results on the presence of the redshifted features initially reported (J. Cottam et al. 2008). Moreover, the observation of quasi-coherent oscillations during type I bursts, indicative of the neutron star's spin at 552 Hz (D. K. Galloway et al. 2010), casts doubts about the photospheric origin of the detected narrow absorption lines, which lack any Doppler broadening consistent with the fast spin.

During the 1980s, there were a few reports of X-ray absorption lines at 4.1 keV during type I X-ray bursts observed with the Tenma and EXOSAT satellites (see I. Waki et al. 1984; N. Nakamura et al. 1988; E. Magnier et al. 1989). These were interpreted as redshifted Lyα absorption from He-like iron at a rest-frame energy of 6.7 keV. In all these cases, the observed absorption line energy of $\sim$4.1 keV implies compactness of the neutron star of $R/M = 3.2$ (using

$G = c = 1$). Despite all these detections, the reality of these lines and their interpretation has been controversial, partly because subsequent observations have not confirmed these claims.

Recent observational studies have revealed narrow emission and absorption features in type I bursts from 4U 1820-30, offering insight into the dynamics of photospheric radius expansion (PRE) events. T. E. Strohmayer et al. (2019) analyzed five PRE bursts observed with NICER in 2017, identifying a discrete emission line near 1.0 keV and narrow absorption lines at ∼1.7 keV and ∼3.0 keV. These absorption features exhibited a systematic blueshift of ∼4.6%, implying expansion velocities of order $v \approx 0.046c$ (∼14,000 km s^{-1}), interpreted as due to burst-driven winds coupled with gravitational redshift effects (T. E. Strohmayer et al. 2019). Subsequently, F. Barra et al. (2025) extended the analysis to 12 PRE bursts, confirming up to four significant absorption lines per burst and consistently detecting an absorption feature at ∼2.97 keV. Together, these observations support a scenario in which heavy-element ashes are lifted into an expanding photospheric shell, producing discrete spectral lines whose blueshifts and strengths trace the dynamics and ionization structure of the burst-driven wind (see also J. J. M. in't Zand & N. N. Weinberg 2010; H. Yu & N. N. Weinberg 2018).

Recent analyses of thermonuclear X-ray bursts from the ultracompact binary 4U 1820-30 have revealed the presence of an absorption feature at approximately 3.8 keV. Z. Peng et al. (2025) observed a redshifted absorption feature at ∼3.6–4 keV in NICER data during the superburst recovery of 4U 1820-30. They attribute it to burning-ash material in the accretion disk —likely Ar XVIII[10]—that becomes visible as the disk moves back inward. A similar feature was independently reported by G. K. Jaisawal et al. (2025), who detected a 3.75 keV absorption line during the aftermath of a long burst event. In this case, the absorption line is attributed to absorption by heavy nuclei in the wind or accretion flow, enriched by nuclear burning products. The authors suggest that elements such as Si, Ar, Ca, or Ti may be responsible for this line, and that the absorption is shaped by both gravitational redshift and Doppler effects from the expanding photosphere.

However, the identification of an isolated absorption feature is intrinsically ambiguous when only a single line is detected. For this reason, here we fit the strong absorption line observed in the aftermath of the superburst from 4U 1820-30 with a self-consistent absorption model and find that it is well described by absorption from highly ionized, gravitationally redshifted iron, with a redshift factor of $1 + z \approx 1.7$. The line is also significantly broadened, with $\Delta E_{\rm FWHM}/E \approx 0.15$, a width that is fully consistent with Doppler broadening due to the neutron star's rotational velocity (assuming a spin frequency of 716 Hz) along the line of sight. We therefore interpret the line as originating from the atmosphere of the neutron star. The redshift of $1 + z \simeq 1.72$ corresponds to a compactness of the neutron star of $\simeq 4.46\ {\rm km}/M_\odot$. If confirmed, this will offer invaluable insights into the EoS of matter at nuclear densities.

[10] It should be noted that the attribution by Peng et al. of the observed feature at 4.15 keV to Ar XVIII is inconsistent, as the rest-frame energy of the Ar XVIII Lyα transition is 3.32 keV. Instead, a transition at 4.1 keV would be consistent with the rest-frame energy of Car XX Lyα.

2. Observations and Analysis

Following the detection of a bright X-ray burst from the position consistent with the low-mass X-ray binary 4U 1820-30 by the Monitor of All-Sky X-ray Image (MAXI; M. Serino et al. 2021) at 11:27 UT on 2021 August 23, NICER initiated follow-up observations to monitor the postburst evolution of the source. During the MAXI/Gas Slit Camera (GSC) scan, the 4–10 keV flux, averaged under the assumption of constant emission, reached 1868^{+104}_{-94} mCrab (1σ uncertainty). In the subsequent scan at 13:01 UT, the flux had decreased to 486 ± 50 mCrab, still above the persistent level of ∼200 mCrab. No significant excess was observed in the previous scan at 09:55 UT, suggesting that the burst onset occurred before the 11:27 UT transit.

NICER (K. C. Gendreau et al. 2016) observed 4U 1820-30 on 2021 August 23 at 14:35:00 UT (ObsID 4050300105, hereafter Obs. 105) and again on August 24 at 06:08:25 UT (ObsID 4050300106, hereafter Obs. 106), with exposures of 25 ks and 52 ks, respectively. The X-ray Timing Instrument on board NICER operates in the 0.2–12 keV range and consists of 56 photon detectors, of which 52 focal plane modules (FPMs) are currently active; four modules (12, 22, 29, and 60) were disabled post-launch due to damage.

Data reduction was carried out using the `nicerl2` pipeline within `NICERDAS` v13, part of the `HEAsoft` v6.34 package (J. K. Blackburn 1995), using standard filtering criteria and calibration database version `xti20240206`. All operational FPMs were active during both observations. Light curves in the 0.5–2 keV and 2–5 keV bands were extracted with `nicerl3-lc`, and corresponding hardness ratios (HRs) were computed.

Figure 1 displays the light curves and HRs for Obs. 105 and Obs. 106. During Obs. 106, the count rate in the 0.5–2 keV band increased from 700 to 1400 cts s^{-1}, while the 2–5 keV band rose from 450 to 600 cts s^{-1}, before decreasing to ∼525 cts s^{-1} at 110 ks from the start. The HR initially dropped steeply from 0.66 to 0.55 in the first 3 ks, followed by a more gradual decline to 0.4.

For Obs. 105 and Obs. 106, light curves from two distinct energy bands and their corresponding HRs are presented in Figure 1. The analysis revealed a count rate increase in the 0.5–2 keV band from 700 to 1.400 cts s^{-1} and in the 2–5 keV band from 450 to 600 cts s^{-1}, before a decrease to 525 cts s^{-1} at 110 ks from the start. The HR showed a steep decline from 0.66 to 0.55 in the first 3 ks, followed by a more gradual decrease to 0.4.

The MAXI light curves of 4U 1820-30, obtained with the GSC in four energy bands from MJD 59446 to MJD 59453 and extracted adopting the method described in S. Nakahira et al. (2012), are showcased in Figure 2. The red and blue vertical lines demarcate the start and end of NICER's Obs. 105, highlighting the superburst's onset approximately 6 hr before Obs. 105 began. This event's impact is notably pronounced in the 4–6 keV, 6–8 keV, and 8–10 keV bands, where the source's intrinsic variability is less dominant. The 2–20 keV MAXI count rate during the NICER observations is 0.92 ± 0.03 cts s^{-1}. Looking at the hardness–intensity diagram of 4U 1820-30 presented by A. Marino et al. (2023), a count rate of 0.92 ± 0.03 cts s^{-1} suggests that the source is in the "banana" state (see, e.g., T. Di Salvo et al. 2023).

Initially, we investigated the averaged spectrum obtained from Obs. 105 employing the `nicerl3-spect` tool and

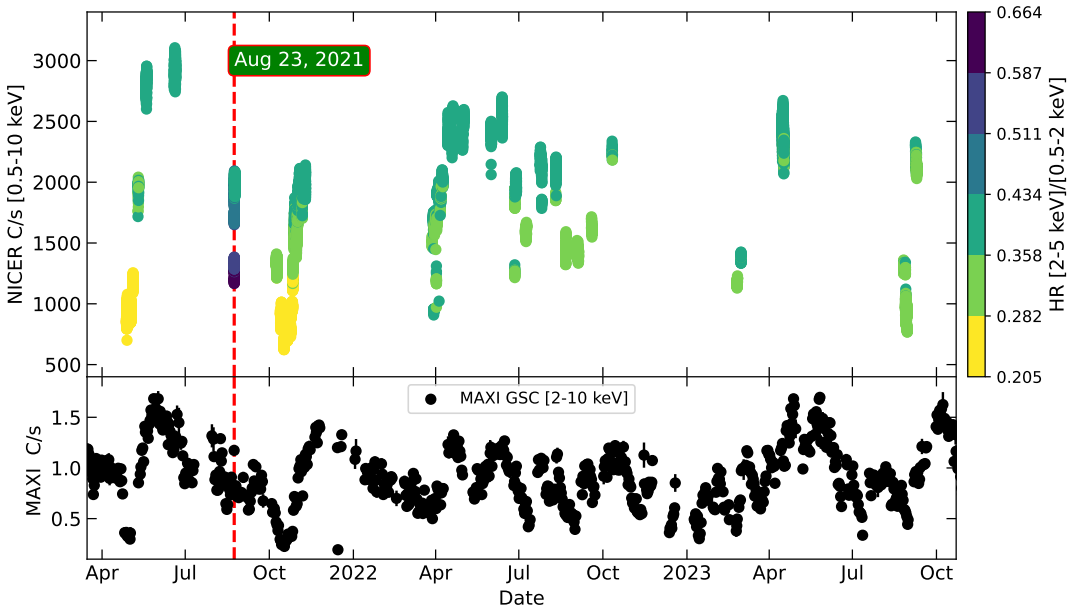

Figure 1. Comparative light curves of 4U 1820-30 from NICER (0.5–10 keV, top) and MAXI/GSC (2–10 keV, bottom). In the NICER panel, color indicates the HR between the [2–5] and [0.5–2] keV bands, ranging from 0.2 to 0.4. A red dashed line marks the observation with peak HR = 0.664. MAXI data show a brief increase in count rate coinciding with the NICER observation window.

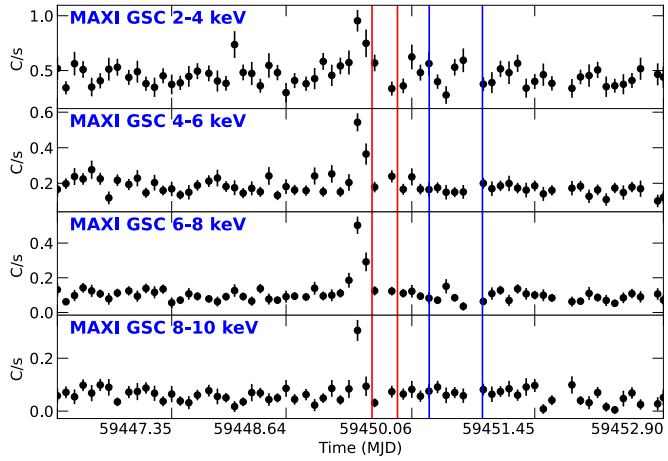

Figure 2. Light curves of the source 4U 1820-30 observed by MAXI in four different energy bands from MJD 59446 to MJD 59453. The vertical lines in red and blue mark the commencement and conclusion of NICER Obs. 105 and 106, respectively. The noticeable surge in the count rate across all selected energy bands correlates with a superburst event, which occurred approximately 6 hr prior to the initiation of NICER Obs. 105.

excluding FPMs 14 and 34 due to their high detector noise levels. This selection criterion prevented possible distortions of the spectral data. The extraction of source spectra and corresponding `scorpeon` background files[11] was performed with `nicerl3-spect`, utilizing the `bkgformat=file` option. In alignment with the NICER calibration team's recommendations for systematic error incorporation,[12] we added a systematic error to all the extracted spectra. In particular, by setting `syserrfile=CALDB` in `nicerl3-spect`, we introduced a systematic error of 1.5% across the 0.4–10 keV energy band. The data were then optimally binned using the `ftgrouppha` tool, applying the `grouptype=optmin` strategy to ensure a minimum of 25 counts per energy bin, as advised by J. S. Kaastra & J. A. M. Bleeker (2016) for statistical robustness in spectral fitting. The exposure time of the spectrum is 8 ks.

2.1. The Averaged Spectrum from Obs. 105

We perform spectral fitting across the 0.4–10 keV energy range of the averaged spectrum obtained from the NICER Obs. 105, using `XSPEC` v12.14.1 and adopting the interstellar abundances of J. Wilms et al. (2000) and the photoelectric cross sections of D. A. Verner et al. (1996a). The baseline model (Model 1) was defined as `TBfeo*(diskbb+thcomp*bbodyrad)`. The `TBfeo` component models interstellar absorption, allowing oxygen and iron abundances to vary. An excess at 0.54–0.56 keV was modeled as an overabundance of neutral oxygen, consistent with previous studies of 4U 1820-30 (E. Costantini et al. 2012).

The `diskbb` component describes multitemperature disk blackbody emission, while `thcomp*bbodyrad` represents Comptonized blackbody emission (see A. A. Zdziarski et al. 2020, for a detailed description of the convolutive component `thcomp`), assuming full coverage (cov = 1) and a fixed electron temperature of 3.1 keV, based on prior broadband studies (A. Marino et al. 2023). The blackbody seed temperature, spectral index Γ, and normalization were left free to vary.

This model yielded a reduced χ^2 of 1.43 for 163 degrees of freedom. Examination of the residuals revealed an absorption feature near 3.8 keV. We first modeled this using a negative Gaussian component (Model 2, `TBfeo*(diskbb+Abs`$_{\rm line}$`+thcomp*bbodyrad)`), which significantly improved the fit. Further refinement included four Gaussian emission lines at fixed energies (identified with transitions of Mg XII, Si XIV, S XV, and Ar XVII, respectively) to account for low-energy residuals (Model 3, `TBfeo*(diskbb+Abs`$_{\rm line}$`+4Em`$_{\rm line}$`+thcomp*bbodyrad)`). The

[11] `scorpeon` background model in XSPEC: https://heasarc.gsfc.nasa.gov/docs/nicer/analysis_threads/scorpeon-xspec/.
[12] NICER calibration guidelines: https://heasarc.gsfc.nasa.gov/docs/nicer/analysis_threads/cal-recommend/.

Table 1
Best-fit Values of the Averaged Spectrum Obtained from Obs. 105

Component	Parameter	Model 1	Model 2	Model 3	Model 4
TBfeo	$N_{\rm H}$	0.172 ± 0.003	0.177 ± 0.005	0.192 ± 0.009	$0.190^{+0.008}_{-0.006}$
	$A_{\rm O}/A_{\rm O}^{\odot}$	1.16 ± 0.07	1.19 ± 0.07	1.24 ± 0.07	1.27 ± 0.08
diskbb	$kT_{\rm disk}$ (keV)	0.70 ± 0.05	0.58 ± 0.04	0.48 ± 0.05	0.53 ± 0.05
	$R_{\rm disk}\sqrt{\cos i}$ (km)	16 ± 2	22 ± 3	31 ± 6	27 ± 4
swind1	$N_{\rm H,wind}$	...	...	...	4^{+3}_{-1}
	$\log(\xi)$	...	...	...	$3.24^{+0.33}_{-0.13}$
	σ (v / c)	...	...	...	0.06 ± 0.02
	z	...	...	...	$0.70^{+0.03}_{-0.02}$
Gaussian	E (keV)	...	3.80 ± 0.04	3.80 ± 0.05	...
	σ (keV)	...	0.24 ± 0.04	0.25 ± 0.05	...
	I ($\times 10^{-2}$)	...	-0.75 ± 0.15	-0.7 ± 0.2	...
thcomp	Γ	$3.3^{+0.4}_{-0.2}$	$2.82^{+0.15}_{-0.11}$	$2.73^{+0.13}_{-0.10}$	3.02 ± 0.13
	kT_e (keV)	(3.1)	(3.1)	(3.1)	(3.1)
bbodyrad	$kT_{\rm bb}$ (keV)	1.23 ± 0.07	1.08 ± 0.05	1.04 ± 0.04	1.12 ± 0.04
	$R_{\rm bb}$ (km)	11.7 ± 1.2	15.2 ± 1.3	16.5 ± 1.5	$14.3^{+1.2}_{-0.8}$
Gaussian	$I_{\rm Mg\ XII}$ ($\times 10^{-2}$)	...	...	1.0 ± 0.6	$1.6^{+0.4}_{-0.6}$
Gaussian	$I_{\rm Si\ XIV}$ ($\times 10^{-2}$)	...	...	1.3 ± 0.5	1.8 ± 0.4
Gaussian	$I_{\rm S\ XV}$ ($\times 10^{-2}$)	...	...	0.4 ± 0.3	0.9 ± 0.3
Gaussian	$I_{\rm Ar\ XVII}$ ($\times 10^{-2}$)	...	...	0.3 ± 0.2	0.6 ± 0.3
χ^2 (dof)		233.1 (163)	109.9 (160)	81.3 (156)	97.6 (155)

Note. The equivalent hydrogen column densities are in units of 10^{22} cm^{-2}. Errors are reported at the 90% confidence level. Values in round parentheses were kept fixed during the fit. The energies and widths of the emission lines were fixed to the values reported in the text.

energies of four emission lines were fixed at their respective rest-frame values: 1.472, 2.006, 2.46, and 3.13 keV. The line widths were fixed at 0.2 keV. The origin of these broad emission lines is consistent with reflection from the inner regions of the accretion disk, where relativistic effects and ionized disk material can produce broadened features at these energies (see A. Anitra et al. 2025).

To evaluate the significance of the broad absorption line, we determined the number of standard deviations by which its normalization deviates from zero. This analysis yielded a significance of 6.1σ. The energy of the absorption line is 3.80 ± 0.05 keV, the width is 0.25 ± 0.05 keV, and the normalization is $(-0.7 \pm 0.2) \times 10^{-2}$ photons cm^{-2} s^{-1}. The equivalent width (EW) of the line was measured to be 44 ± 7 eV, with its uncertainty reported at a 68% confidence level.

In order to identify the 3.8 keV absorption line, we substituted the Gaussian line with a physically motivated model incorporating the swind1 component (M. Gierliński & C. Done 2006) to represent partially ionized absorption with velocity shear (Model 4, TBfeo * (diskbb+4Em$_{\rm line}$+ swind1 * thcomp * bbodyrad)). swind1 describes a partially ionized absorbing material with large velocity shear, approximated using XSTAR kn5 photoionization absorption model grids (calculated assuming a microturbulent velocity of 100 km s^{-1}) and then convoluted with Gaussian smearing. swind1 is defined by four parameters: the ionization state of the absorber ($\xi = L/nR^2$, where L, n, and R are the X-ray luminosity, particle density, and distance of the cloud from the ionizing source, respectively), which can change in response to the variability of the illuminating continuum; the hydrogen column density ($N_{H_{\rm wind}}$), which can change as clouds move in and out of the line of sight; the velocity shear, parameterized by the width of the smearing Gaussian (σ in units of v/c), which can also change; and finally, the redshift (z).

This model yielded a best-fit χ^2 of 97.6 for 155 degrees of freedom (dof). The inclusion of the swind1 component successfully accounted for the broad absorption feature without the need for an ad hoc Gaussian and without leaving any residuals that might indicate model-predicted features not present in the observed spectrum. Furthermore, the multiplicative swind1 component was applied to the Comptonized emission in order to mimic the presence of an ionized absorber located near the neutron star surface.

The observed disk and blackbody temperatures, $kT_{\rm disk}$ and $kT_{\rm bb}$, are 0.53 ± 0.05 keV and 1.12 ± 0.04 keV, respectively. Using the obtained blackbody normalization values and assuming a distance of 8.0 ± 0.3 kpc to 4U 1820-30's host, the globular cluster NGC 6624 (H. Baumgardt & E. Vasiliev 2021), we calculated the inner radius of the accretion disk, uncorrected for the inclination angle i, as $R_{\rm disk}\sqrt{\cos i} = 27 \pm 4$ km. Similarly, the blackbody radius $R_{\rm bb}$ was determined to be $14.3^{+1.2}_{-0.8}$ km.

The large blackbody radius suggests that the seed photons for the Comptonized cloud originate from the neutron star surface and the boundary layer. The power-law photon index of the Comptonization is $\Gamma = 3.02 \pm 0.13$. Having fixed the electron temperature of the Comptonizing cloud at 3.1 keV, this corresponds to an optical depth $\tau = 6.0 \pm 0.4$.

Finally, the equivalent hydrogen column density of the ionized absorbing matter responsible for the broad absorption line observed in the spectrum is $N_{H_{\rm wind}} = (4^{+3}_{-1}) \times 10^{22}$ cm^{-2}. The ionization parameter is $\log(\xi) = 3.24^{+0.33}_{-0.13}$, and the Gaussian sigma for velocity smearing is 0.06 ± 0.02 in units of v/c, corresponding to a velocity of 17100^{+4800}_{-4200} km s^{-1}. The model also gives a significant redshift of $z = 0.70^{+0.03}_{-0.02}$, indicating that the line is fitted with a transition from the K-shell of iron ions.

All model parameters and fit statistics are summarized in Table 1. The unfolded spectra and the residuals for Models 1

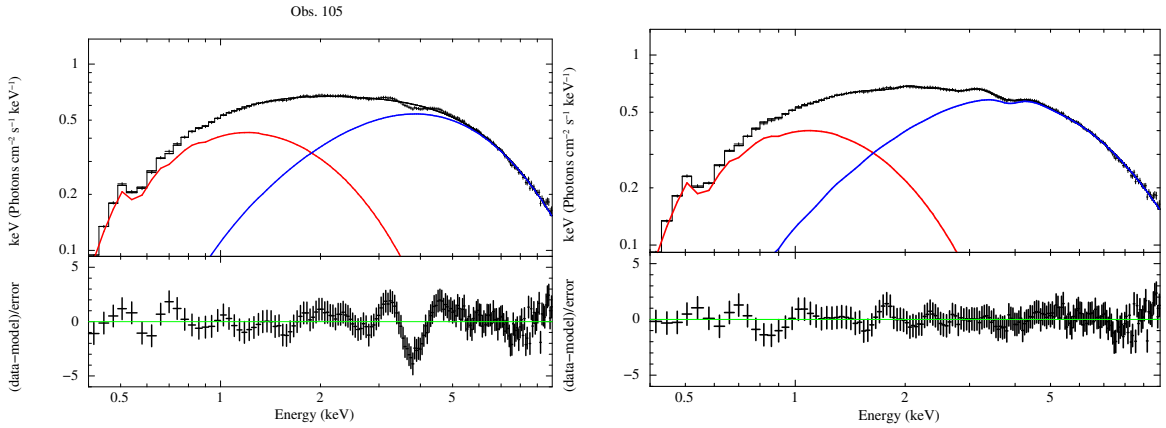

Figure 3. Unfolded spectrum and residuals in units of σ for the averaged spectrum obtained from the NICER Obs. 105, adopting Model 1 (left panel) and Model 4 (right panel). The thermal emission from the accretion disk and the Comptonized component are in red and blue, respectively.

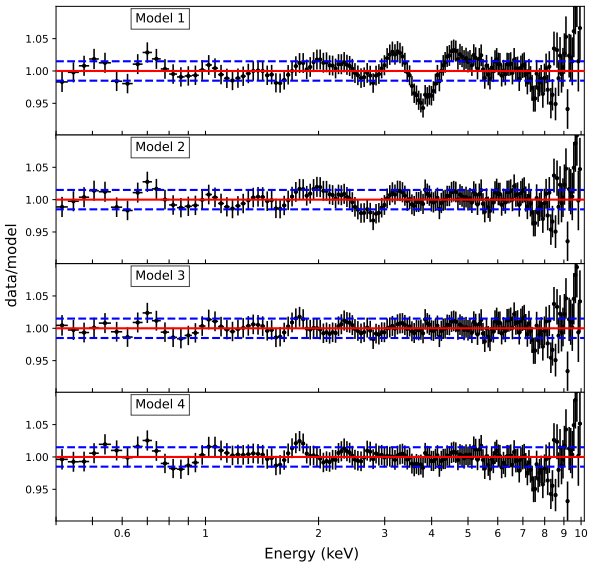

Figure 4. Data-to-model ratios of the averaged spectrum extracted from Obs. 105, adopting Model 1, Model 2, Model 3, and Model 4 (from top to bottom, respectively). The dashed blue lines indicate a ratio of 1.5%, corresponding to the systematic error associated with the spectrum.

and 4 are shown in Figure 3, while the residuals and data-to-model ratios for all four models are presented in Figure 4.

2.2. Temporal Evolution of the Spectrum

The HR evolution in NICER data reveals significant spectral variability during Obs. 105 and Obs. 106. To study the spectral evolution, we divided the observations into seven temporal intervals (five for Obs. 105 and two for Obs. 106), as shown in Figure 5. The exposure times of the extracted spectra are listed in Table 2. For each segment, we extracted a spectrum and applied Model 4. The resulting best-fit parameters are listed in Table 3. Residuals are shown in Figure 6, and the evolution of key parameters is illustrated in Figure 7.

The equivalent hydrogen column density of the ionized absorber remains stable within uncertainties. The blackbody temperature ($kT_{\rm bb}$) shows a monotonic decline from 1.4 to 0.8 keV, while its radius ($R_{\rm bb}$) increases across the observation from 10 to 30 km. Disk temperature ($kT_{\rm disk}$) and radius ($R_{\rm disk}\sqrt{\cos i}$) remain approximately constant at 0.55 keV and 25 km, respectively.

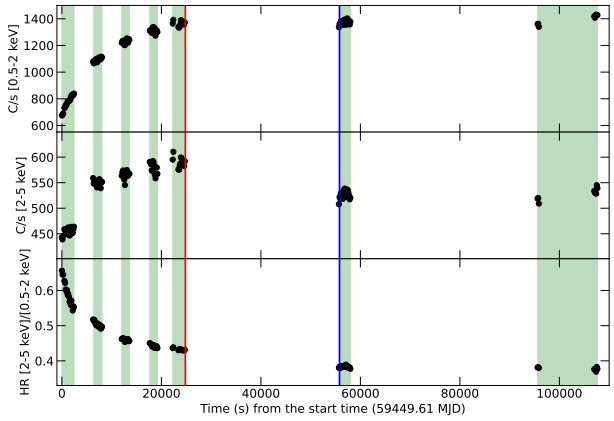

Figure 5. NICER light curves for Obs. 105 and Obs. 106 in the 0.5–2 keV (top) and 2–5 keV (middle) bands. The bottom panel shows the HR. Green shaded regions mark intervals used for spectral extraction; red and blue lines indicate the end of Obs. 105 and the start of Obs. 106, respectively.

Table 2
Selected Intervals from the NICER Observations

Interval	Start (s)	Stop (s)	Exp. (s)
1	0	2600	2284
2	6300	8200	1716
3	12,000	14,000	1586
4	17,500	19,500	1463
5	22,000	25,000	1454
6	55,820	58,120	2212
7	95,000	109,000	897

Note. Times are referenced to the beginning of Obs. 105 (MJD 59449.61).

Each spectrum includes a significantly broad absorption feature near 3.8 keV. Its detection significance, assessed by removing the `swind1` component from the model, ranges from 2.5σ to over 8σ, as shown in Figure 8 (red points). The absorption is stronger in intervals 2–4 and becomes marginal in interval 7.

The absorbing ionized matter responsible for the broad absorption line is constrained between $5 \times 10^{22}\,{\rm cm}^{-2}$ and $1.0 \times 10^{23}\,{\rm cm}^{-2}$ and remains unchanged within the errors throughout the entire observation. The ionization parameter,

Table 3
Best-fit Values of the Seven Spectra Adopting Model 4

Component	Parameter	Int. 1	Int. 2	Int. 3	Int. 4	Int. 5	Int. 6	Int. 7
TBfeo	$N_{\rm H}$ (1022 cm^{-2})	0.186 ± 0.010	0.188 ± 0.007	$0.189^{+0.006}_{-0.009}$	0.183 ± 0.007	$0.181^{+0.015}_{-0.005}$	$0.182^{+0.015}_{-0.007}$	$0.188^{+0.016}_{-0.005}$
	$A_O/A_O^{\odot}$	1.34 ± 0.09	1.27 ± 0.08	1.31 ± 0.09	1.22 ± 0.08	$1.22^{+0.15}_{-0.08}$	$1.28^{+0.10}_{-0.13}$	$1.29^{+0.10}_{-0.04}$
diskbb	$kT_{\rm disk}$ (keV)	$0.52^{+0.07}_{-0.02}$	$0.56^{+0.08}_{-0.05}$	$0.54^{+0.08}_{-0.04}$	$0.60^{+0.05}_{-0.09}$	$0.60^{+0.06}_{-0.10}$	$0.66^{+0.10}_{-0.08}$	0.5 ± 0.12
	$R_{\rm disk}\sqrt{\cos i}$ (km)	23 ± 5	24 ± 5	27 ± 5	24^{+7}_{-3}	24^{+10}_{-4}	21 ± 4	28^{+12}_{-2}
swind1	$N_{H_{\rm wind}}$	3^{+5}	5^{+4}_{-2}	7^{+4}_{-2}	7^{+5}_{-3}	5^{+5}_{-2}	5^{+7}_{-2}	3^{+4}
	$\log(\xi)$	3.8 ± 0.3	$3.28^{+0.22}_{-0.14}$	$3.25^{+0.23}_{-0.11}$	$3.25^{+0.25}_{-0.12}$	$3.2^{+0.4}_{-0.6}$	$2.9^{+0.8}_{-0.3}$	2.5 ± 0.3
	σ (v / c)	$0.057^{+0.022}_{-0.015}$	0.060 ± 0.014	0.052 ± 0.010	0.059 ± 0.014	0.06 ± 0.02	(0.06)	(0.06)
	z	0.71 ± 0.05	0.64 ± 0.03	0.72 ± 0.02	0.73 ± 0.02	0.76 ± 0.03	$0.80^{+0.06}_{-0.05}$	$0.83^{+0.17}_{-0.08}$
thcomp	Γ	8^{+2}_{-3}	$4.0^{+0.7}_{-0.5}$	$2.94^{+0.35}_{-0.07}$	$2.69^{+0.15}_{-0.19}$	$2.34^{+0.15}_{-0.07}$	$2.13^{+0.13}_{-0.10}$	$1.93^{+0.11}_{-0.02}$
	kT_e (keV)	(3.1)	(3.1)	(3.1)	(3.1)	(3.1)	(3.1)	(3.1)
bbodyrad	$kT_{\rm bb}$ (keV)	$1.40^{+0.02}_{-0.04}$	$1.21^{+0.06}_{-0.04}$	$1.07^{+0.06}_{-0.02}$	1.05 ± 0.08	$0.98^{+0.11}_{-0.07}$	0.9 ± 0.2	$0.76^{+0.30}_{-0.07}$
	$R_{\rm bb}$ (km)	9.5 ± 0.6	12.7 ± 1.0	$16.0^{+1.2}_{-2.0}$	16 ± 3	18^{+4}_{-2}	18^{+8}_{-4}	27^{+24}_{-4}
Gaussian	$I_{\rm Mg\ XII}$ ($\times 10^{-2}$)	0.8 ± 0.5	1.5 ± 0.5	2.0 ± 0.6	1.4 ± 0.6	$1.1^{+0.8}_{-0.3}$	$0.6^{+0.6}_{-0.4}$	<0.6
Gaussian	$I_{\rm Si\ XIV}$ ($\times 10^{-2}$)	1.1 ± 0.3	$2.2^{+0.2}_{-0.4}$	2.0 ± 0.5	1.5 ± 0.4	$1.2^{+0.5}_{-0.4}$	0.8 ± 0.4	<0.7
Gaussian	$I_{\rm S\ XV}$ ($\times 10^{-2}$)	$0.24^{+0.14}_{-0.19}$	$1.0^{+1.0}_{-0.2}$	0.6 ± 0.3	0.4 ± 0.2	0.3 ± 0.3	<0.3	<0.2
Gaussian	$I_{\rm Ar\ XVII}$ ($\times 10^{-2}$)	$0.4^{+0.2}_{-0.3}$	1.6 ± 0.5	1.0 ± 0.4	0.7 ± 0.5	0.3 ± 0.2	<0.3	<0.2
χ^2 (dof)		80.7 (144)	111.1 (143)	116.6 (143)	87.5 (143)	95.3 (143)	68.8 (146)	74.7 (138)

Note. Column densities are in units of 10^{22} cm^{-2}. Errors are quoted at the 90% confidence level. Values in parentheses were kept fixed during fitting. Intensities are given in units of photons cm^{-2} s^{-1}. The energies and widths of the emission lines were fixed to the values reported in the text.

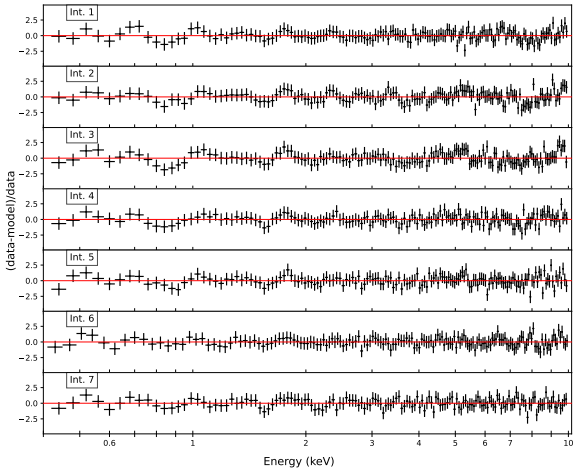

Figure 6. Residuals, expressed in units of σ, for the seven spectra extracted from Obs. 105 and Obs. 106, following temporal segmentation and modeled using Model 4.

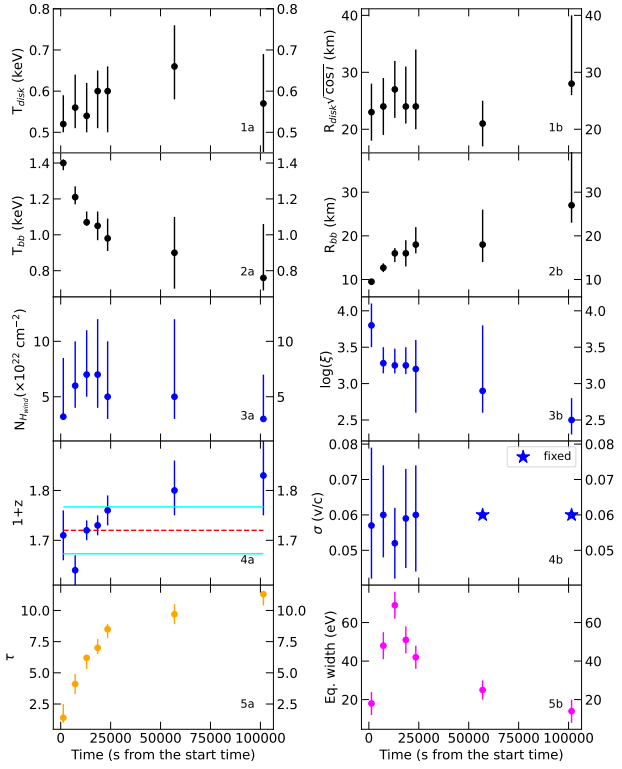

Figure 7. Temporal evolution of the best-fit spectral parameters using Model 4. The panels show the inner disk temperature (1a) and radius (1b); blackbody temperature (2a) and radius (2b); Compton cloud optical depth τ (5a); and for the swind1 component, column density (3a), ionization parameter (3b), redshift (4a), and velocity smearing σ (4b). Panel (5b) shows the EW (in eV) of the broad absorption line derived using Model 3. Errors in all parameters are quoted at the 90% confidence level, except for the EW in panel (5b), which is shown with a 68% confidence level.

$\log(\xi)$, decreases steadily throughout the observation. It starts at 3.8 ± 0.3 in the first interval, drops to 3.2 during intervals 2 to 5, decreases further to 2.9 in interval 6, and finally, reaches 2.5 in interval 7.

The redshift exhibits a general increase from 0.7 to 0.8, with the exception of interval 2, where it drops to 0.64 ± 0.03. For the first five spectra obtained from Obs. 105, the best-fit values are consistent with $z \approx 0.70$, in agreement with the result from the analysis of the averaged spectrum. In contrast, the best-fit values from Obs. 106 are closer to 0.8, albeit with larger associated uncertainties. Assuming a constant temporal behavior, we determine a redshift of $1 + z = 1.72 \pm 0.05$ at the 99.7% confidence level.

The optical depth of the Comptonized component, inferred from the parameter Γ using Equation (14) in A. A. Zdziarski et al. (2020), increases progressively from 1.4 to 11.3 throughout the observation.

By adopting Model 3 to fit the seven spectra, we inferred that the EW (in eV) of the broad absorption line varies across the intervals, with values of 18 ± 6, 48 ± 7, 69 ± 7, 51 ± 7,

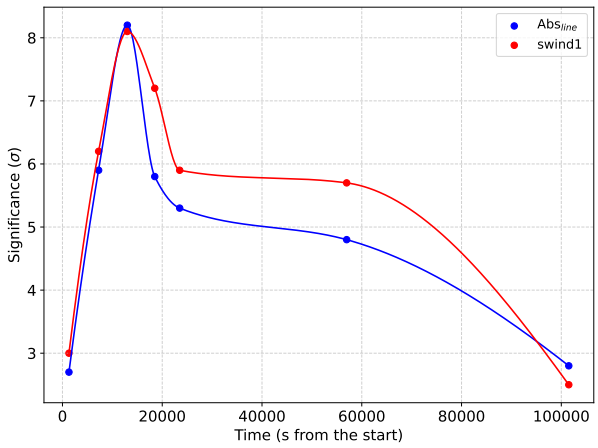

Figure 8. The significance, expressed in units of standard deviation, is shown for Model 4 (`swind1` component, red points) and Model 3 (Gaussian component, blue points), respectively. The absorption feature is barely significant in interval 7.

42 ± 6, 25 ± 5, and 14 ± 6 from interval 1 through interval 7, respectively (see panel (5b) in Figure 7). All quoted uncertainties correspond to a 68% confidence level. The detection significance, evaluated by excluding the Gaussian absorption line from the model, ranges from 2.5σ to over 8σ, as illustrated in Figure 8 (blue points). The absorption feature is most prominent in intervals 2–4 and becomes marginal in interval 7, consistent with the trend observed using Model 4.

3. Constraint on the Photospheric Iron Mass Fraction from the EW

The measurement of the EW of the broad absorption line provides a quantitative constraint on the mass fraction of iron in the neutron star photosphere. In the linear part of the curve of growth, the rest-frame EW $W_{\lambda,0}$ is related to the ionic column density N_i by the following relation:

$$W_{\lambda,0} = \frac{\pi e^2}{m_e c^2} N_i f \lambda_0^2 = \pi r_e N_i f \lambda_0^2, \quad (1)$$

(see, e.g., R. Iaria et al. 2007a, and references therein) where e is the elementary charge, m_e the electron mass, c the speed of light, r_e the classical electron radius, λ_0 the rest-frame wavelength of the transition, and f the oscillator strength. Using the standard values of these quantities gives $\pi r_e \simeq 8.85 \times 10^{-13}$ cm. Since $W_\lambda/\lambda \simeq W_E/E$, the observed equivalent width can be written as $W_{\lambda,\rm obs} = \lambda_{\rm obs}^2/(hc)\, W_{E,\rm obs}$, where $\lambda_{\rm obs}$ is the observed wavelength of the transition and $W_{E,\rm obs}$ the measured EW of the broad absorption line. Transforming to the rest frame yields

$$W_{\lambda,0} = \frac{\lambda_{\rm obs}^2}{hc} \frac{W_{E,\rm obs}}{1+z}. \quad (2)$$

Combining Equations (1) and (2), we obtain

$$N_i = \frac{(1+z)\, W_{E,\rm obs}}{\pi r_e\, hc\, f}, \quad (3)$$

where $hc \simeq 1.24 \times 10^{-4}$ eV cm. Adopting a gravitational redshift of $1 + z = 1.72$, we find $N_i \simeq 1.57 \times 10^{16}\, W_{E,\rm obs}[\rm eV]/f$ cm^{-2}. Using oscillator strengths from D. A. Verner et al. (1996b), $f = 0.798$ for Fe XXV and $f = 0.416$ for Fe XXVI, and an observed EW range of 15–60 eV, we derive N_i(Fe XXV) $\simeq (2.9 \times 10^{17}$–$1.2 \times 10^{18})$ cm^{-2} and N_i(Fe XXVI) $\simeq (5.7 \times 10^{17}$–$2.3 \times 10^{18})$ cm^{-2}. Equation 3 assumes the optically thin, linear curve-of-growth limit. In burst atmospheres, resonant line transport and departures from LTE can modify the mapping between EW and ionic column density (L. Bildsten et al. 2003; P. Chang et al. 2005); therefore the inferred N_i should be regarded as an order-of-magnitude estimate.

Assuming that the line forms over a layer of thickness L comparable to the pressure scale height ($H \simeq 2.5$ cm at $kT \simeq 1$ keV, $g \simeq 2 \times 10^{14}$ cm s^{-2}, and a mean molecular weight $\mu = 1.3$ for a He-dominated atmosphere, as expected for 4U 1820-303) and adopting an ionization fraction $f_{\rm ion} = 0.4$–0.6 consistent with the observed $\log \xi \simeq 3.2$–3.8 (see, e.g., Figure 5 in T. R. Kallman et al. 2004), the total iron number density is

$$n_{\rm Fe,tot} = \frac{N_i}{f_{\rm ion} L}. \quad (4)$$

The corresponding iron mass fraction is then

$$X_{\rm Fe} = \frac{A m_p N_i}{f_{\rm ion} L \rho_{\rm tot}}, \quad (5)$$

where the atomic mass number A for iron is 56, m_p is the proton mass, and $\rho_{\rm tot}$ the photospheric density. For a helium-rich atmosphere radiating at $F/F_{\rm Edd} \simeq 0.2$, appropriate for the postsuperburst epoch considered here, we adopt $\rho_{\rm tot} \simeq 0.44/(F/F_{\rm Edd}) \simeq 2$ g cm^{-3} (see, e.g., V. Suleimanov et al. 2011).

Taking representative values of $W_E = 50$ eV, $L \simeq 3$ cm, and $f_{\rm ion} = 0.5$, we obtain $X_{\rm Fe} \approx 3 \times 10^{-5}$ and $X_{\rm Fe} \approx 6 \times 10^{-5}$ for Fe XXV and Fe XXVI, respectively. Thus, the inferred iron mass fraction at the line-forming depth is $X_{\rm Fe} \simeq (3$–$6) \times 10^{-5}$, consistent (within a factor of 2) with the solar iron abundance $A_{\rm Fe,\odot} = 2.7 \times 10^{-5}$ (J. Wilms et al. 2000).

Finally, the independently fitted warm-absorber column $N_{\rm H,wind} \simeq (0.3$–$1.2) \times 10^{23}$ cm^{-2} implies an Fe column of $(0.8$–$3.2) \times 10^{18}$ cm^{-2} for solar composition, in excellent agreement with the ionic columns inferred from the EW analysis. We therefore conclude that solar or mildly enhanced iron abundances in the accreted atmosphere are sufficient to reproduce the observed line strength, and that no substantial enrichment from superburst ashes is required.

4. Possible Neutron Star Compactness Constraints

The fitting of the absorption line with Model 4 implies a significant redshift that we interpret as a gravitational redshift. The gravitational redshift is described by the equation

$$1 + z = [1 - 2GM/(c^2 R)]^{-1/2},$$

where G is the gravitational constant, c is the speed of light, M is the neutron star mass, and R is the neutron star radius from which the photons are emitted. The value of $1 + z$ allows us to estimate the neutron star compactness; by adopting the best-fit value of $1 + z$ of 1.72 ± 0.05 (99.7% confidence level), we infer a neutron star compactness of 4.46 ± 0.13 km$/M_\odot$ (or 3.02 ± 0.09 in units of $G = c = 1$).

Recent work by G. K. Jaisawal et al. (2024) on thermonuclear X-ray bursts from 4U 1820-30, observed with NICER,

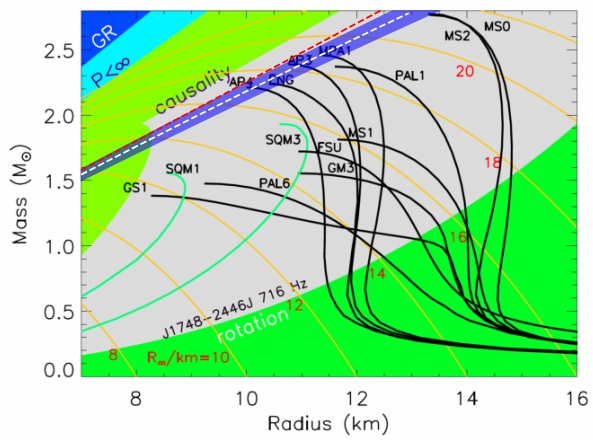

Figure 9. Mass–radius diagram for neutron stars. Black (hadronic EOSs) and green (strange quark matter) curves represent common equations of state (see J. M. Lattimer & M. Prakash 2001). The red dashed line shows the best-fit compactness $R/M = 3.02 \pm 0.09$, inferred from a redshift of $1 + z = 1.72 \pm 0.05$ (99.7% confidence) for a nonrotating neutron star. The white dashed line accounts for rotation at 716 Hz. The blue-shaded area reflects the uncertainty in redshift. The green area (upper left) is causally excluded; the lower right is excluded by the fastest known pulsar. Adapted from J. M. Lattimer & M. Prakash (2016).

reported a potential spin frequency of 716 Hz, with a significance of 2.9σ. Assuming this spin frequency and an inclination angle of 31° (A. Anitra et al. 2025), we can estimate the neutron star compactness in its rotating state. To achieve this, we consider the Schwarzschild geometry, perturbed to account for a nonzero angular velocity Ω while assuming that the object is rigid enough to neglect the quadrupole moment and apply the Newtonian approximation for the angular momentum: $2/5MR^2\Omega$.

As rotation breaks spherical symmetry, off-diagonal terms appear in the metric. The relation between the gravitational redshift is then given by

$$(1 + z)^{-1} = (-g_{tt} - 2g_{t\phi}\Omega - \Omega^2 g_{\phi\phi})^{1/2},$$

as shown in Equation (9) of P. D. Nuñez & M. Nowakowski (2010).

Using the perturbative method up to the third order of the Butterworth–Ipser metric (E. M. Butterworth & J. R. Ipser 1976; see also Equation (33) in P. D. Nuñez & M. Nowakowski 2010) and neglecting the quadrupole moment, we numerically determine the mass as a function of the radius for a neutron star with a spin frequency of 716 Hz, an inclination angle of 31°, and a gravitational redshift of $1 + z = 1.72 \pm 0.05$.

Fitting our solutions with a quadratic function, we obtain the following relation:

$$\frac{M}{M_\odot} = (-1.64 \pm 0.03) \times 10^{-3}\left(\frac{R}{1\ \mathrm{km}}\right)^2 + (0.240 \pm 0.007)\left(\frac{R}{1\ \mathrm{km}}\right) - (0.062 \pm 0.001). \quad (6)$$

We present the mass–radius relation without accounting for the neutron star rotation, shown as a dashed red line in Figure 9. The mass–radius relation indicated by a dashed white line takes into account the proposed neutron star rotation. The errors, derived from the uncertainty in the gravitational redshift, are represented by the blue-shaded region.

Adopting the inferred compactness, we can constrain the radius and mass of 4U 1820-30, assuming a maximum neutron star gravitational mass of 2.3 $M_\odot$ (Y.-Z. Fan et al. 2024). The lower limit of the radius is set by the causality condition, which restricts it to values above 8.3 km (see Figure 9), while the upper limit of 11 km is constrained by assuming a neutron star mass of 2.3 $M_\odot$. For a radius of 8.3 km, the corresponding lower mass limit is 1.8 $M_\odot$. Therefore, the neutron star mass is constrained between 1.8 and 2.3 $M_\odot$, while the radius lies within the range of 8.3–11 km.

Absorption lines are routinely detected in high-inclination low-mass X-ray binaries (LMXBs; e.g., L. Boirin & A. N. Parmar 2003; Y. Ueda et al. 2004; M. Díaz Trigo et al. 2006; R. Iaria et al. 2007a, 2007b; G. Ponti et al. 2012; R. Iaria et al. 2021). These features are typically very narrow, with full width at half-maximum (FWHM) less than a few 10^2–10^3 km s^{-1} (i.e., $\Delta E/E < 10^{-3}$, corresponding to <1–10 eV at 6–7 keV), and therefore lie well below the usual spectral resolution of CCD-class X-ray instruments and are often only marginally resolved even with gratings. The lines are widely interpreted as originating in photoionized accretion disk winds, and their small widths are most likely set by turbulence and/or velocity shear/dispersion within the outflow (e.g., M. Díaz Trigo & L. Boirin 2016). On the other hand, the absorption line discussed here is significantly broad, with a Gaussian $\sigma \simeq 0.25$ keV, compatible with the velocity dispersion inferred from the `swind1` model of $\sigma/E \simeq 0.06$ in units of v/c. We show that this value is compatible even with a neutron star spin at 716 Hz. In fact, using the best-fit value for the velocity dispersion inferred from the absorption line width, $\sigma = 0.06 \pm 0.02\ v/c$, we derive a corresponding velocity dispersion expressed as the half width at half-maximum that is $\Delta v \sin i = 21,200 \pm 7,000$ km s^{-1}, where i is the inclination angle of the source, which is compatible with the broadening that would be induced by the neutron star rotation if we assume an inclination angle of 31°. In fact, at the neutron star surface, the tangential velocity is expected to follow the relation $v = 2\pi\nu R$, where ν is the neutron star spin frequency, and R is the neutron star radius. Considering the extreme values of the estimated neutron star radius range, $R = 8.3$ km and $R = 11$ km, and a neutron star spin frequency of 716 Hz, we obtain a projected velocity along the line of sight of 19,200 and 25,500 km s^{-1}, respectively. These values are perfectly consistent with the velocity dispersion inferred from the width of the absorption line.

5. Discussion

We report on the study of a pronounced and transient absorption feature in the range of 3.6–3.9 keV within the NICER spectrum of the ultracompact LMXB 4U 1820-30, where a weakly magnetized neutron star accretes matter from a helium white dwarf companion in an extremely close orbit. This feature emerged in the NICER data recorded on 2021 August 23, a few hours after the occurrence of a superburst, and persisted for nearly 60 ks before vanishing.

In the recent literature, the only comparable observation is a transient absorption edge at 3.8 keV identified in the spectrum of the prompt X-ray emission from the gamma-ray burst GRB 990705, as captured by the Gamma-ray Burst Monitor and Wide Field Cameras on board the X-ray satellite BeppoSAX (L. Amati et al. 2000). This phenomenon was effectively modeled as iron photoelectric absorption by a medium at a

redshift of approximately 0.86, with an iron abundance roughly 75 times that of the solar level. On the other hand, the absorption feature observed in 4U 1820-30 is not consistent with an absorption edge; instead, it closely fits a Gaussian absorption line profile, suggesting its identification with an iron transition line.

Absorption lines similar to those discussed in this paper were identified in the 1980s with the Tenma and EXOSAT satellites. Three separate studies (see I. Waki et al. 1984; N. Nakamura et al. 1988; E. Magnier et al. 1989), each examining a different LMXB system (4U 1636-536, 4U 1608-522, EXO 1747-214, respectively), reported a pronounced absorption line around 4 keV, interpreted as a 6.7 keV iron line redshifted by the neutron star gravitational field. In every instance, the line was detected during type I bursts, with evidence suggesting a lesser redshift at the outburst's peak—presumably when the neutron star atmosphere expands due to the thermonuclear explosion. Specifically, in 4U 1636-536 (see I. Waki et al. 1984), the line appeared at 5.7 keV at the burst peak, decreasing to 4.1 keV as the burst waned. These observations imply a high neutron star compactness, yielding an R/M ratio of 3.2. Despite these findings, the existence of these lines and their interpretations have sparked controversy, partly because subsequent observations have not confirmed these claims. Moreover, the EW of these absorption lines was of the order of hundreds of eV, which theoretical models of spectral formation in burst atmospheres could not reproduce (A. J. Foster et al. 1987; C. S. R. Day et al. 1992). The absorption line we measure in 4U 1820-30 has a moderate and more reasonable EW between 15 and 60 eV.

In all the cases previously mentioned, the line was detected during a type I burst and, in a few instances, at the burst peak. A more recent study (N. M. Barrière et al. 2015) reported a weak absorption line at 5.46 keV at the peak of a type I burst, adding to the evidence. In contrast, we observe the line well after the occurrence of the superburst. Fitting the line with a photoionization absorption model (`swind1` in the `XSPEC` package) implies a redshift of 1.72 ± 0.05 (99.7% confidence level). Such a redshift is consistent with the line origin from iron ions at the neutron star surface. From the redshift of the line, we can directly estimate the compactness of the star in the range $R/M \simeq 4.46 \pm 0.13\ \mathrm{km}/M_{\odot}$, which indicates a mass for the neutron star larger than $1.8\,M_{\odot}$ according to the representative modern EOS (see Figure 9, adapted from J. M. Lattimer & M. Prakash 2016).

The emission profile of a spectral line from the rapidly rotating surface of a neutron star typically manifests as a single-peak Gaussian under the assumption of uniform emission across the entire star. With an increase in spin frequency, the line tends to weaken and broaden, and its peak emission shifts to higher energies, reflecting the rotational dynamics of the neutron star (F. Özel & D. Psaltis 2003). Line profile asymmetry is accentuated when the emission is restricted to a portion of the stellar surface, a scenario often associated with young neutron stars that exhibit lateral composition and temperature gradients due to intense magnetic fields, leading to an asymmetric, double-peaked profile (e.g., S. Bhattacharyya et al. 2006). The absorption line observed in 4U 1820-30 presents a Gaussian profile, suggesting that the emission encompasses the entire (or a significant portion of the) neutron star surface.

The obtained compactness was estimated assuming a static neutron star. However, the mass–radius relation must account for rapid rotation if the spin frequency of 716 Hz suggested by G. K. Jaisawal et al. (2024) is confirmed. Using a gravitational redshift of 1.72 ± 0.05, a spin frequency of 716 Hz, and an inclination angle of 31° (A. Anitra et al. 2025), we estimated the mass–radius relation of the neutron star using the Butterworth–Ipser metric (E. M. Butterworth & J. R. Ipser 1976). This approach applies the perturbative method up to the third order, neglecting the quadrupole term and assuming a moment of inertia of $2/5MR^2$ (see Equation (33) in P. D. Nuñez & M. Nowakowski 2010). The mass–radius relation for a rotating neutron star with a spin frequency of 716 Hz is presented as a white dashed line in Figure 9. The associated uncertainty, driven by the gravitational redshift, is illustrated as the blue-shaded region.

To infer an estimate of the redshift of the absorption line, we applied the `swind1` model to the Comptonized component. The best-fit redshift value obtained from this model ($1 + z = 1.72 \pm 0.05$) enables us to estimate a neutron star compactness of $4.46 \pm 0.13\ \mathrm{km}/M_{\odot}$ or 3.02 ± 0.09 in dimensionless units ($G = c = 1$).

Using the `swind1` model, we find that plausible combinations of parameters can reproduce a strong, redshifted iron absorption line without introducing other prominent spectral features, such as an associated Fe edge, that would otherwise be expected. However, the precise identification of this absorption line requires accurate knowledge of the chemical composition of the neutron star photosphere following a carbon superburst. Indeed, alternative identifications have been proposed in the literature. For example, Z. Peng et al. (2025) interpret the line as arising from Ar XVIII (or Ca XX) originating in the inner accretion disk, while G. K. Jaisawal et al. (2025) suggest that it could be due to neutral Ti or H-like Ca, both cases implying moderate gravitational redshifts.

We note, however, that the NICER observation was performed approximately 3 hr after the superburst detected by MAXI, and it is therefore reasonable to assume that the wind driven by the burst's high luminosity had already subsided. In addition, the analysis of the line EW, combined with the inferred absorber column density, indicates iron abundances consistent (within a factor of 2) with solar values. Thus, the line does not require any significant enhancement in the abundances of heavy elements. In this scenario, the superburst plays a crucial *indirect* role: the radiation-driven phase associated with the burst removes or substantially thins the accretion corona, temporarily exposing the neutron star photosphere. As the wind fades and the photosphere returns to its equilibrium radius, the continuum emerging from the stellar surface passes through its own thin, highly ionized atmosphere, allowing the detection of the broad iron absorption line gravitationally redshifted to ∼3.8 keV. As the Comptonizing corona gradually reforms around the neutron star, the absorption line becomes progressively weaker, consistent with the decrease in its EW as the optical depth of the corona increases and the ionization parameter of the absorber decreases.

Future instruments with larger collecting areas, such as Athena and eXTP (X. Barcons et al. 2017; P. S. Ray et al. 2018; J. J. M. in't Zand et al. 2019), which possess the capability for higher throughput and/or improved spectral resolution in the classical X-ray range of 1–10 keV, could offer

new tools for more precise line identifications. These advancements may facilitate the use of such line detections to measure the compactness of neutron stars accurately. Meanwhile, NICER, thanks to its large effective area in the soft X-ray range, is leading to groundbreaking findings in neutron star physics, particularly through the precise measurement of the mass and radius of neutron stars such as PSR J0030+0451 and PSR J0740+6620. For PSR J0030+0451, two independent analyses using the pulse-profile modeling approach have determined the neutron star mass to be approximately 1.3–1.4 $M_{\odot}$ with a radius of about 13 km (M. C. Miller et al. 2019; T. E. Riley et al. 2019). For PSR J0740+6620, the inferred gravitational mass of 2.08 $\pm$ 0.07 $M_{\odot}$ is the highest reliably determined mass for any neutron star thus far. The equatorial circumferential radius was found to be around 13.7 km (M. C. Miller et al. 2021). In line with that, our results on 4U 1820-30 point toward another massive neutron star, albeit with a possible smaller radius. Indeed, by using the canonical mass value of 1.4 $M_{\odot}$ in the compactness we infer from the redshifted absorption line, we obtain a radius for the neutron star of 6.4 $\pm$ 0.2 km. Conversely, by setting a radius of 10 km, we derive a mass of 2.18 $\pm$ 0.06 $M_{\odot}$. Confirming these results would provide essential constraints on the EoS characterizing ultra-dense matter, further enriching our understanding of the extreme conditions within neutron stars.

6. Software and Third-party Data Repository Citations

This work made use of the following standard software tools and repositories:

1. `XSPEC` v12.14.1 for spectral fitting (K. A. Arnaud 1996);
2. `HEASoft` v6.34, including `NICERDAS` and `FTOOLS`, for data reduction and analysis;
3. `CALDB` (NICER calibration database, version xti20240206).
4. Public NICER data from the HEASARC archive: Observation IDs 4050300105 and 4050300106.

No proprietary or custom software was used in this work.

Acknowledgments

R.I. and T.D.S. acknowledge support from PRIN-INAF 2019 with the project "Probing the geometry of accretion: from theory to observations" (PI: Belloni). W.L. acknowledges the PhD program in PhD in Space Science and Technology at the University of Trento, Cycle XXXVIII. A.A. acknowledges financial support from ASI-INAF Accordo Attuativo HERMES Pathfinder operazioni n. 2022-25-HH.0

Facilities: NICER, MAXI (GSC).

Software: XSPEC (K. A. Arnaud 1996), HEASoft (https://heasarc.gsfc.nasa.gov/docs/software/heasoft/), NICERDAS (https://heasarc.gsfc.nasa.gov/docs/nicer/analysis_threads/), CALDB (https://heasarc.gsfc.nasa.gov/docs/heasarc/caldb/caldb_intro.html).

Author Contribution

R.I. and T.D.S. led the spectral analysis, data interpretation, and writing of the manuscript. A.A., F.B., A.S., and L.B. contributed to the data interpretation and/or modeling. All authors contributed to the review and editing of the manuscript.

ORCID iDs

R. Iaria https://orcid.org/0000-0003-2882-0927
T. Di Salvo https://orcid.org/0000-0002-3220-6375
A. Anitra https://orcid.org/0000-0002-2701-2998
F. Barra https://orcid.org/0000-0001-5852-6740
A. Sanna https://orcid.org/0000-0002-0118-2649
C. Maraventano https://orcid.org/0009-0007-8593-5006
C. Miceli https://orcid.org/0009-0005-1240-6985
W. Leone https://orcid.org/0000-0002-4773-3370
L. Burderi https://orcid.org/0000-0001-5458-891X

References

Abbott, B. P., Abbott, R., Abbott, T. D., et al. 2017, PhRvL, 119, 161101
Amati, L., Frontera, F., Vietri, M., et al. 2000, Sci, 290, 953
Anitra, A., Gnarini, A., Di Salvo, T., et al. 2025, A&A, 697, A83
Arnaud, K. A. 1996, ASPC, 101, 17
Barcons, X., Barret, D., Decourchelle, A., et al. 2017, AN, 338, 153
Barra, F., Barret, D., Pinto, C., et al. 2025, A&A, 694, A266
Barrière, N. M., Krivonos, R., Tomsick, J. A., et al. 2015, ApJ, 799, 123
Baumgardt, H., & Vasiliev, E. 2021, MNRAS, 505, 5957
Bhattacharyya, S., Miller, M. C., & Lamb, F. K. 2006, ApJ, 644, 1085
Bildsten, L., Chang, P., & Paerels, F. 2003, ApJ, 591, L29
Blackburn, J. K. 1995, ASPC, 77, 367
Boirin, L., & Parmar, A. N. 2003, A&A, 407, 1079
Butterworth, E. M., & Ipser, J. R. 1976, ApJ, 204, 200
Chang, P., Bildsten, L., & Wasserman, I. 2005, ApJ, 629, 998
Costantini, E., Pinto, C., Kaastra, J. S., et al. 2012, A&A, 539, A32
Cottam, J., Paerels, F., & Mendez, M. 2002, Natur, 420, 51
Cottam, J., Paerels, F., Méndez, M., et al. 2008, ApJ, 672, 504
Day, C. S. R., Fabian, A. C., & Ross, R. R. 1992, MNRAS, 257, 471
Di Salvo, T., Papitto, A., Marino, A., Iaria, R., & Burderi, L. 2023, in Handbook of X-ray and Gamma-ray Astrophysics, ed. C. Bambi & A. Santangelo (Springer), 147
Díaz Trigo, M., & Boirin, L. 2016, AN, 337, 368
Díaz Trigo, M., Parmar, A. N., Boirin, L., Méndez, M., & Kaastra, J. S. 2006, A&A, 445, 179
Fan, Y.-Z., Han, M.-Z., Jiang, J.-L., Shao, D.-S., & Tang, S.-P. 2024, PhRvD, 109, 043052
Foster, A. J., Ross, R. R., & Fabian, A. C. 1987, MNRAS, 228, 259
Galloway, D. K., Lin, J., Chakrabarty, D., & Hartman, J. M. 2010, ApJL, 711, L148
Gendreau, K. C., Arzoumanian, Z., Adkins, P. W., et al. 2016, SPIE, 9905, 99051H
Gierliński, M., & Done, C. 2006, MNRAS, 371, L16
Iaria, R., di Salvo, T., Lavagetto, G., D'Aí, A., & Robba, N. R. 2007a, A&A, 464, 291
Iaria, R., Lavagetto, G., D'Aí, A., di Salvo, T., & Robba, N. R. 2007b, A&A, 463, 289
Iaria, R., Sanna, A., Di Salvo, T., et al. 2021, A&A, 646, A120
in't Zand, J. J. M., Bozzo, E., Qu, J., et al. 2019, SCPMA, 62, 29506
in't Zand, J. J. M., & Weinberg, N. N. 2010, A&A, 520, A81
Jaisawal, G. K., Bostancı, Z. F., Boztepe, T., et al. 2024, ApJ, 975, 67
Jaisawal, G. K., Chenevez, J., Strohmayer, T. E., et al. 2025, ApJ, 986, 16
Kaastra, J. S., & Bleeker, J. A. M. 2016, A&A, 587, A151
Kallman, T. R., Palmeri, P., Bautista, M. A., Mendoza, C., & Krolik, J. H. 2004, ApJS, 155, 675
Lattimer, J. M., & Prakash, M. 2001, ApJ, 550, 426
Lattimer, J. M., & Prakash, M. 2016, PhR, 621, 127
Magnier, E., Lewin, W. H. G., van Paradijs, J., et al. 1989, MNRAS, 237, 729
Marino, A., Russell, T. D., Del Santo, M., et al. 2023, MNRAS, 525, 2366
Miller, M. C., Lamb, F. K., Dittmann, A. J., et al. 2019, ApJL, 887, L24
Miller, M. C., Lamb, F. K., Dittmann, A. J., et al. 2021, ApJL, 918, L28
Nakahira, S., Koyama, S., Ueda, Y., et al. 2012, PASJ, 64, 13
Nakamura, N., Inoue, H., & Tanaka, Y. 1988, PASJ, 40, 209
Nuñez, P. D., & Nowakowski, M. 2010, JApA, 31, 105
Özel, F., & Freire, P. 2016, ARA&A, 54, 401
Özel, F., & Psaltis, D. 2003, ApJL, 582, L31
Peng, Z., Li, Z., Pan, Y., et al. 2025, ApJ, 982, 18
Ponti, G., Fender, R. P., Begelman, M. C., et al. 2012, MNRAS, 422, L11
Ray, P. S., Arzoumanian, Z., Brandt, S., et al. 2018, SPIE, 10699, 1069919
Riley, T. E., Watts, A. L., Bogdanov, S., et al. 2019, ApJL, 887, L21
Serino, M., Iwakiri, W., Negoro, H., et al. 2021, ATel, 15071, 1

Strohmayer, T. E., Altamirano, D., Arzoumanian, Z., et al. 2019, ApJL, 878, L27
Suleimanov, V., Poutanen, J., & Werner, K. 2011, ApJ, 527, A139
Ueda, Y., Murakami, H., Yamaoka, K., Dotani, T., & Ebisawa, K. 2004, ApJ, 609, 325
Verner, D. A., Ferland, G. J., Korista, K. T., & Yakovlev, D. G. 1996a, ApJ, 465, 487
Verner, D. A., Verner, E. M., & Ferland, G. J. 1996b, ADNDT, 64, 1
Waki, I., Inoue, H., Koyama, K., et al. 1984, PASJ, 36, 819
Wilms, J., Allen, A., & McCray, R. 2000, ApJ, 542, 914
Yu, H., & Weinberg, N. N. 2018, ApJ, 863, 53
Zdziarski, A. A., Szanecki, M., Poutanen, J., Gierliński, M., & Biernacki, P. 2020, MNRAS, 492, 5234